Dynamic Field Map Estimation Using a Spiral-In/Spiral-Out Acquisition

Bradley P. Sutton,* Douglas C. Noll, and Jeffrey A. Fessler

The long readout times of single-shot acquisitions and the high field strengths desired for functional MRI (fMRI) using blood oxygenation level-dependent (BOLD) contrast make functional scans sensitive to magnetic field inhomogeneity. If it is not corrected during image reconstruction, field inhomogeneity can cause geometric distortions in the images when Cartesian *k*-space trajectories are used or blurring with spiral acquisitions. Many traditional methods to correct for field inhomogeneity distortions rely on a static field map measured with the use of images that are themselves distorted. In this work, we employ a regularized least-squares approach to jointly estimate both the undistorted image and field map at each acquisition using a spiral-in/spiral-out pulse sequence. Simulation and phantom studies show that this method is accurate and stable over a time series. Human functional studies show that the jointly estimated field map may be more accurate than standard field map estimates in the presence of respiration-induced phase oscillations, leading to better detection of functional activation. The proposed method measures a dynamic field map that accurately tracks magnetic field drift and respiration-induced phase oscillations during the course of a functional study. Magn Reson Med 51:1194–1204, 2004. © 2004 Wiley-Liss, Inc.

Key words: image reconstruction; field inhomogeneity; functional MRI; iterative methods; spiral

Functional imaging using blood oxygenation level-dependent (BOLD) contrast is performed by acquiring T_2^*-weighted images using gradient-echo acquisitions during task and rest (1). The gradient-echo acquisitions typically are fast, single-shot techniques such as EPI or spiral imaging. Single-shot techniques allow high temporal resolution and avoid the mixing of respiratory phases or subject motion between the shots in a multishot acquisition. However, the long readout times of single-shot acquisitions make them sensitive to magnetic field inhomogeneities that can lead to severe distortions in the images. Magnetic field inhomogeneities exist around regions where materials with different magnetic susceptibility come into contact, for example at air/tissue interfaces. When these effects are not corrected, they can cause geometric distortions when EPI scans are used, and blurring with spiral acquisitions. The artifacts due to field inhomogeneity can cause problems when functional results are obtained from areas near air/tissue interfaces. Spatial distortions can also degrade the accuracy of image registration algorithms for motion correction, or for aligning functional results to anatomical images.

Many image reconstruction methods have been proposed to correct for field distortions in spiral imaging (e.g., Refs. 2–6). There are two steps involved in most field inhomogeneity correction schemes. The first is to measure the spatial variation of the magnetic field (this is referred to as "estimating the field map"). The second step is to use that field map to compensate for field inhomogeneities during the reconstruction. Several methods have been presented that bypass the first step. For example, Noll et al. (3) used an autofocusing criterion based on the assumption that the phase is locally smoothly varying in a field-corrected image. However, most field correction methods rely on obtaining a good estimate of the field map.

Conventionally, the field map is measured by acquiring two images at slightly different echo times (TEs) and dividing their phase difference by the difference in TEs (7). The difference in TEs must be kept small (a few milliseconds) to avoid problems with 2π phase wraps when the phase differences between the two images are calculated. Determining the difference in TEs for a specific pixel from two separate acquisitions is not completely straightforward. If the same pulse sequence is used to acquire the image twice with only a difference in TE, then the effective TE difference for the two images is that difference in TEs. If a different sequence is used to acquire the data at two different TEs, then the influence of underlying gradients of the field inhomogeneity must be taken into account to determine the effective TE (i.e., the time at which the origin of *k*-space is acquired) (8). This effective TE may vary on a pixel-by-pixel basis (8).

To acquire images at two closely spaced TEs, a multiecho gradient-echo pulse sequence could be used. This would result in relatively undistorted images, but it could also require a significant amount of scan time. More often, a faster technique that acquires two single-shot images is used to acquire a field map just prior to acquisition of the functional study. This eliminates the problem of registering the field map to the functional images. We will refer to this method as the "standard field map estimation method." The standard field map estimation method assumes implicitly that all of the off-resonance phase accrual occurs at the TE, and ignores dephasing during the data readout, which may be longer than the TE. If the images used to measure the field map are taken with the same acquisition parameters that are to be used in the imaging study, they are distorted by field inhomogeneities and the resulting field map suffers from the image distortions.

For a standard field map estimation, the TEs of the two reference images must be within a few milliseconds of

Department of Biomedical Engineering, University of Michigan, Ann Arbor, Michigan.

Bradley P. Sutton is now at the Beckman Institute for Advanced Science and Technology, University of Illinois at Urbana-Champaign, Urbana, Illinois.

*Correspondence to: Brad Sutton, 2100 S. Goodwin Ave., Urbana, IL 61801. E-mail: bsutton@uiuc.edu

each other to avoid ambiguity in the field map measurement that would result from 2π phase wraps. Given that the total acquisition time for a single-shot image is tens of milliseconds, one must use two separate acquisitions (TR intervals) to acquire two images with slightly different TEs. Respiration-induced phase variations in the two reference images, other physiological noise, or subject motion between the two acquisitions can lead to errors in the standard field map estimate. For example, in our scans, the center frequency of an axial slice can vary by 1 Hz depending on the position in the respiratory cycle. This could result in a phase difference of as much as (2πTE $\times$ 1 Hz) radians between the two acquisitions, even in the absence of additional field inhomogeneity. This phase difference divided by the difference in TEs could induce a 15-Hz error in the field map estimate for a TE of 30 ms and a TE delay of 2 ms. For the spiral scans used in this work, the PSF amplitude is reduced by one-half for an off-resonance of 32 Hz, but substantial blurring occurs for off-resonance values of roughly 15 Hz or larger. Therefore, errors in the standard field map estimate due to respiration can lead to significant artifact in the reconstructed image.

Field maps resulting from standard estimates are usually assumed to be static over the course of a functional study because an additional scan with a delayed TE is required. This additional scan is usually performed at the beginning or end of a functional study. This one measured field map is used to correct the entire time series of images. However, dynamic changes in the field map for a slice can occur during the course of a functional study. These changes can be due to respiratory-cycle-induced phases, main field drift, and subject motion. When field-corrected image reconstruction algorithms are used, these dynamic changes can lead to further distortions in the images for a time series. Nayak et al. (9) and Nayak and Nishimura (10) presented a method to form standard, dynamic estimates of a low-resolution field map by delaying TEs of subsequent shots in a multishot experiment. However, these estimates are sensitive to the differences in reference images discussed in the previous paragraph, whereas the method we will propose here estimates the field map within a single acquisition.

This work describes a new way to combine the two steps employed for field inhomogeneity correction used in conjunction with a certain pulse sequence. We propose to reconstruct an undistorted image and its associated dynamic, undistorted field map from a spiral-in/spiral-out acquisition. This method retains the time resolution and other benefits of single-shot methods while it corrects for distortions caused by the changing field map. The spiral-in/spiral-out pulse sequence can acquire the same number of slices per TR as a spiral-out sequence (11), and thus should not change the setup of current functional MRI (fMRI) studies.

THEORY

We approach the simultaneous estimation problem by forming a cost function based on the signal equation for MRI and then minimizing it over the image and field map simultaneously. First we present our cost function based on the signal equation in terms of the unknown image and field map, and then we discuss our minimization process.

Nonlinear Least-Squares Joint Estimation

In MRI, the equation for the complex baseband signal, ignoring relaxation effects, is given by

$$s(t) = \int f(r)e^{-i\omega(r)t}e^{-i2\pi(k(t)\cdot r)}\,dr, \qquad [1]$$

where $s(t)$ is the signal at time t during the readout, $f(r)$ is a function of the object's transverse magnetization at location r, $\omega(r)$ is the field inhomogeneity, and $k(t)$ is the k-space trajectory. In an MR scan, the raw measurements are noisy samples of this signal,

$$y_m = s(t_m) + \varepsilon_m, \quad m = 1, \dots, M, \qquad [2]$$

and from these samples we would like to simultaneously estimate the image, $f(r)$, and the field map, $\omega(r)$.

This is clearly an ill-posed problem, since there is an infinite collection of solutions, $f(r)$ and $\omega(r)$, that closely match the data $y = (y_1, \dots, y_m)$. We proceed by parameterizing the object and field map in terms of basis functions as follows:

$$f(r) \approx \sum_{n=0}^{N-1} f_n\phi_1(r - r_n)$$

$$\omega(r) \approx \sum_{n=0}^{N-1} \omega_n\phi_2(r - r_n). \qquad [3]$$

For the results presented here, we use the voxel indicator function $\phi_1(r) = \phi_2(r) = rect(r_1/\Delta_{r_1}) \cdots rect(r_P/\Delta_{r_P})$ for the P-dimensional problem. This choice is natural for the object, $f(r)$, since the display device will use square areas of nearly constant luminance; however, better choices for the field map, $\omega(r)$, may exist that would allow for the modeling of within-voxel nonuniformity of the magnetic field intensity. Alternative basis functions will be explored in a future work. Substituting Eq. [3] in Eq. [1] yields

$$s(t) \approx \Phi(k(t)) \sum_{n=0}^{N-1} f_n e^{-i\omega_n t}e^{-i2\pi(k(t)\cdot r_n)}, \qquad [4]$$

where $\Phi(k(t))$ results from the Fourier transform of $\phi(r)$, i.e., $sinc(k_1(t)\Delta_{r_1}) \cdots sinc(k_P(t)\Delta_{r_P})$. We express the noisy measured samples of this signal in matrix-vector form as follows:

$$y = A(\omega)f + \varepsilon, \qquad [5]$$

where $f = (f_0, \dots, f_{N-1})$ and the elements of the $M \times N$ matrix $A(\omega)$ are

$$a_{m,n}(\omega) = \Phi(k(t_m))e^{-i\omega_n t_m}e^{-i2\pi k(t_m)\cdot r_n}. \qquad [6]$$

Our goal is to estimate the image, f, and the field map, ω, from the k-space data y, accounting for the statistics of the noise ϵ.

In Ref. 12, we used the formulation in Eq. [5] as part of an inverse problem approach to field-inhomogeneity-corrected image reconstruction (i.e., estimate the image f given the field map, ω). We showed that in regions with large field inhomogeneity, the iterative reconstruction method results in more accurate images than the standard conjugate phase approach. However, this accuracy may be limited by errors in the estimated field map. In Ref. 12, a static field map from an additional scan was used. Because of the size of the system matrix A, it is impractical to directly calculate its inverse, and it is usually ill-conditioned anyway. Instead, we used the iterative method of conjugate gradients (CG). The main operations involved in the CG method are computing Ax and A^*y, i.e., evaluating Eq. [4] and a complex conjugate transpose version of that equation. We developed accurate approximations to speed the computation of these two matrix-vector products: the nonuniform fast Fourier transform (NUFFT) (13) and a min-max optimal interpolator for time segmentation (12). In this work, we propose to estimate both the image and the field map, and we will use both of these speed-up methods extensively.

Since the dominant noise in a single image for MRI is white Gaussian (14), we can estimate f and ω by minimizing the following penalized least-squares cost function:

$$\Psi(f, \omega) = \frac{1}{2} \|y - A(\omega)f\|^2 + \beta_1 R(f) + \beta_2 R(\omega) \text{ so that,}$$

$$\hat{f}, \hat{\omega} = \arg \min_{f,\omega} \Psi(f, \omega). \qquad [7]$$

The second half of the equation for $\Psi(f, \omega)$ includes regularization terms, $R(f)$ and $R(\omega)$, that penalize the roughness of the estimated image and field map. The parameter β_1 is chosen to control noise but not to significantly affect the resolution of the problem. For the regularization of the field map, β_2 is chosen to result in a relatively smooth field map, similar to the standard field map estimates obtained after smoothing. For simplicity, we used a quadratic regularization, $R(f) = \frac{1}{2}\|Cf\|^2$ for a matrix C that takes differences between neighboring pixels.

Implementation: Nonlinear Estimation Problem

The minimization problem (Eq. [7]) requires an iterative algorithm. We alternate between updating $\hat{f}$ and $\hat{\omega}$. First we update the image given the current estimate of the field map, and then we update the field map given the new estimate of the image. To update the image, we exploit the linear relation between the image and the data, and apply the iterative conjugate gradient (CG) algorithm for minimization of Eq. [7] over f. Once we have updated our estimate of the image, $\hat{f}$, we use gradient descent on the cost function Ψ from Eq. [7] to update the estimate of the field map, $\hat{\omega}$. The gradient of Ψ with respect to ω is given by

$$\frac{\partial}{\partial \omega_n} \Psi(\omega) = \frac{1}{2} g_n(\omega) + \frac{1}{2} g_n^*(\omega) + \frac{\partial}{\partial \omega_n}\beta_2 R(\omega), \qquad [8]$$

where we define $g_n(\omega)$ as follows:

$$g_n(\omega) = -i \sum_{m=1}^{M} t_m f_n^* \Phi^*(k(t_m)) e^{i(2\pi k(t_m) \cdot r_n + \omega_n t_m)}(y_m - [A(\omega)f]_m).$$

$$[9]$$

We formulate the gradients based on the vector g given by,

$$g(\omega) = -iD(f^*)A^*(\omega)D(t)(y - A(\omega)f), \qquad [10]$$

where $D(x)$ denotes a diagonal matrix with the elements of the vector x on its diagonal. Inserting the vector g and using our chosen regularization function $R(\omega)$, we can express the gradient of Ψ with respect to ω as follows:

$$\nabla_\omega \Psi = \frac{1}{2} (g(\omega) + g^*(\omega)) + \beta_2 C' C\omega$$
$$= Real\{g(\omega)\} + \beta_2 C' C\omega, \qquad [11]$$

Using the gradient in Eq. [11], we update our estimate of the field map, ω^k, by gradient descent:

$$\omega^{k+1} = \omega^k - \alpha(Real\{g(\omega^k)\} + \beta_2 C' C\omega^k). \qquad [12]$$

The step size α is chosen such that the cost function, Ψ, decreases.

MATERIALS AND METHODS

In principle, one could apply the estimation method described above to any k-space trajectory. However, the quality of the results will certainly be trajectory-dependent. The spiral-in/spiral-out sequence was chosen because it provides efficient coverage of k-space and a close spacing of TEs. A spiral-in/spiral-out pulse sequence was used in simulation, phantom, and human experiments with the following parameters: TE/FA/FOV = 30 ms/60°/24 cm, matrix size = 64 × 64, and a 1-ms gap between the end of the spiral-in part of the pulse sequence and the beginning of the spiral-out portion. We performed all field-corrected image reconstructions using the fast, iterative technique described in Ref. 12 on the entire spiral-in/spiral-out data. This was done so that differences in the reconstructed images would be due only to differences in the field maps, and not to differences in the reconstruction or regularization. We reconstructed the uncorrected images using a fast gridding operation on the spiral-in and spiral-out portions separately. The resulting images were then combined via a square root of the average of the squares of the images.

The computations of Ax and A^*y in Eq. [10] were carried out with the NUFFT and time segmentation algorithms described in Refs. 12 and 13. These methods dramatically speed computation of the iterative methods while they do not explicitly store the system matrix, which can be large. Time segmentation is used to calculate the phase due to field inhomogeneities at the endpoints of a limited number of time segments over the readout interval and interpolate to get the phase at intermediate points, as described in Ref. 2. The NUFFT is used to compute the signal equation at

arbitrary *k*-space locations using the fast Fourier transform (FFT) and local interpolation. Time segmentation was performed with the use of $L = 8$ time segments. The NUFFT used a 5×5 interpolation neighborhood and two times oversampling for the FFT. Standard estimates for the field maps are usually smoothed to reduce noise. We performed a small amount of smoothing of the standard field map estimates within the object being imaged, and extended the field map beyond the object using a penalized, weighted least-squares smoothing function (15).

Simulation Study

Simulation data sets were formed from a high-resolution brain scan with its associated field map at a matrix size of $256 \times 192 \times 128$, and then reconstructed at a lower resolution (matrix = 64×64) for the reconstructed slice. Noise was added to the data to give an SNR ($\|$data$\|/\|$noise$\|$) of approximately 100.

First, a simulation study was performed to determine the number of subiterations needed to update the image and the field map. This simulation study was performed with slight perturbations of either the image or the field map. First, the image was shifted vertically by one pixel and scaled by 0.9. This initial image, along with the true field map, was fed to the CG algorithm, and 100 subiterations were performed for the image update. The normalized root mean squared error (NRMSE) was used to evaluate accuracy of the reconstruction. The number of subiterations needed to update the image was chosen by finding the point at which the NRMSE reached within 15% of its value at 100 subiterations (near convergence). A similar procedure was used to determine the number of subiterations needed to update the field map. We perturbed the field map by shifting it vertically by one pixel and globally subtracting 2 Hz. The number of subiterations needed to update the field map was chosen as the number at which the NRMSE reached 15% greater than its value at convergence.

Next, we performed a simulation study to determine the number of iterations of the joint estimation algorithm to account for small, dynamic changes in the field map and image that occur between time points in a functional time series. Using the numbers of subiterations for the subloops of the algorithm found above, we performed perturbations on both the image and the field map, and determined the total number of iterations of the joint estimation algorithm by finding the point at which the maximum of the NRMSE in the field map and image estimations dropped to within 15% of its value at 100 iterations. This will be the number of iterations used between time points for the reconstruction of a time series of images.

For the first time point in a functional time series, the standard field map estimate and image reconstructed using that estimate may have a large error. Therefore, a larger number of total iterations may be necessary for the joint estimation method to approach convergence. To determine the number of total iterations required to reconstruct the first time point, we started the algorithm with two initial conditions. First, the algorithm was started with an initial estimate of the field map of zeros. This was used to test how fast the algorithm would converge to the correct field map when starting from a distant point. Second, the algorithm was initialized with the standard estimate of the field map. The standard field map estimate we are using is from two acquisitions at slightly different TEs, as described in the Introduction. For the standard estimate, an additional scan was simulated at a TE delayed by 2 ms. The time of 2 ms was chosen because it is short enough to prevent 2π phase wrap, but is long enough to allow for significant phase accrual due to off-resonance. We used the average of the standard field maps from the spiral-in sequence at the two TEs and the spiral-out sequence at the two TEs as the standard field map. This convention was used in both the simulations and the human experiments. We examined the performance of our joint estimation over iteration using the NRMSE from the true field map.

Human Studies

The human data sets were collected on a GE 3T Signa Scanner (GE Medical Systems, Milwaukee, WI) in accordance with the Institutional Review Board of the University of Michigan. A standard 3D spoiled gradient-recalled (SPGR) sequence was used to acquire a T_1-weighted reference image of each slice examined. Three normal human subjects performed a functional task consisting of four cycles of on/off bilateral finger-tapping, with each cycle lasting 40 s. The subjects were instructed to keep their head still during the functional studies. One human study (subject 1) was performed with a TR of 2 s, yielding 80 time points. Two other human studies (subjects 2 and 3) were acquired with a TR of 0.5 s to allow for good resolution of the respiratory waveform, which causes small shifts in the field map of axial slices. A respiratory bellows was used to acquire the respiratory waveform for these two subjects. Reconstructions using the dynamic, jointly estimated field maps were qualitatively compared to the reconstructions using the static, standard estimates of the field maps. In addition, we compared functional results using the time series of images reconstructed with each field map estimate using the number of active voxels at a given threshold (i.e., the number of voxels with a correlation coefficient with the sinusoidal task waveform that exceeded a given threshold). The time series of the field map estimates were also examined. We scanned a phantom using the same sequence with a TR of 2 s and compared it to the human study to examine variance of the estimate and drifts in the magnetic field. The time series of the higher temporal resolution human studies were compared to the respiratory waveform as measured by the respiratory bellows. A correlation test was performed to assess whether the proposed joint estimation method accurately reflected the respiration-induced phase variations.

RESULTS

Simulation Study

Figure 1 shows the axial and sagittal slices used in the simulations and their associated field maps. The axial slice was used to determine the optimal number of subiterations for the image update and field map update subroutines. Figure 2 shows the NRMSE over subiteration after either
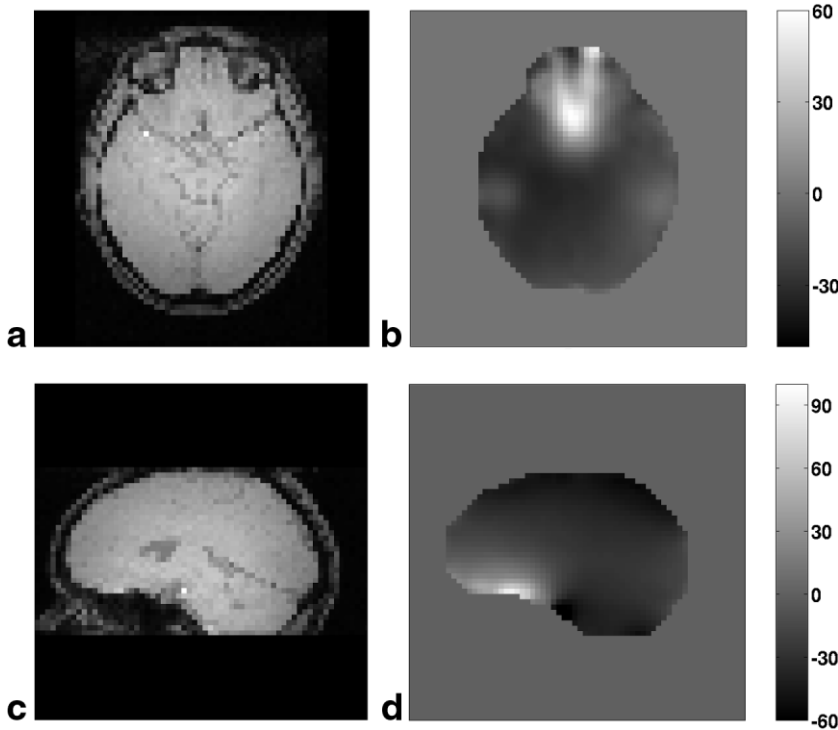
FIG. 1. Objects used for simulation study: (**a**) axial slice, (**b**) axial field map (Hz), (**c**) sagittal slice, and (**d**) sagittal field map (Hz).

the image or the field map was perturbed as described in Materials and Methods. The number of subiterations to use for each update was set to the level at which the NRMSE reached within 15% of its value at 100 subiterations. The number of subiterations of the conjugate gradient method needed to update the image was found to be 6. The number of subiterations of steepest descent needed to update the field map was found to be 19.

Using these numbers of subiterations, we perturbed both the image and the field map as described in Methods and Materials (the NRMSE vs. iteration is shown in Fig. 3 for the image and the field map). The number of total iterations of the simultaneous estimation method needed to account for small dynamic changes was set to be the point at which the NRMSE reached within 15% of its value at 100 iterations. This was found to be 5.

To examine the number of iterations needed to get an initial accurate estimate of the image and field map for a time series, a simulation study was performed with two different initialization conditions and both the axial and sagittal simulation objects from Fig. 1. Figures 4 and 5 show the NRMSE in the field map estimate over iteration for the axial and sagittal studies, respectively, for both of the initialization conditions discussed in Materials and Methods. Both of these sets of curves show that the simultaneous estimation algorithm converges quickly: in about 20 iterations, its NRMSE is <15% greater than its value at 100 iterations. The stability of the joint estimation method is also shown by these figures (i.e., when the algorithm reaches an estimate close to the local minimum, it stays near that minimum). This suggests that an efficient way to implement the simultaneous estimation algorithm for time series data is to initialize the field map for the first time point with the standard, static estimate of the field map,
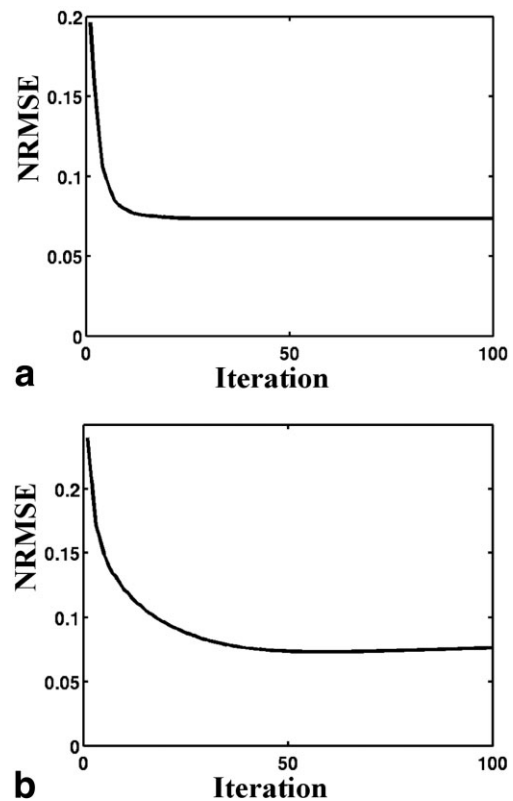

FIG. 2. NRMSE over subiteration for the image and field map, updating subroutines of the joint estimation code. **a:** Perturbing the image by a vertical shift of one pixel and a scaling, but providing the true field map. **b:** Perturbing the field map by a vertical shift and an intensity shift, but providing the true image.
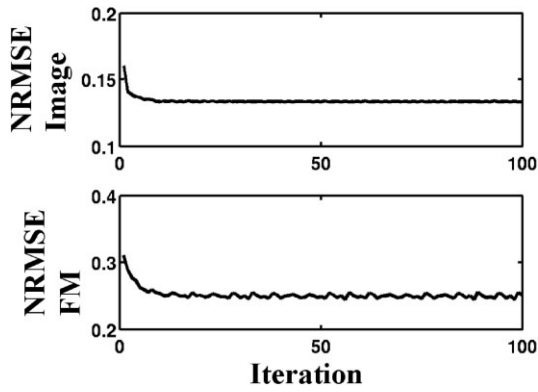
FIG. 3. NRMSE over iteration for perturbed image and field map using five subiterations of CG to update the image and 19 subiterations of steepest descent to update the field map.

and run 20 iterations to account for errors in the standard estimation. Then for each subsequent time point, five iterations are run to account for dynamic changes.

Figures 4 and 5 include the standard field map estimate for reference. The error for the simultaneous estimation algorithm is approximately half that of the standard field map estimate. This is despite the use of two acquisitions of spiral-in/spiral-out for the standard estimate compared to one for the simultaneous estimation. Figure 6 shows the map of the error in our estimate for the sagittal simulation. Comparing this error to the sagittal slice in Fig. 1, we can see that the error occurs near a peak in the field map at the edge of the object. Since the field map outside of the object is initialized to a low value, the quadratic regularization has smoothed out the peak at the edge of the object. The use of a regularization scheme (other than quadratic), such as a Huber penalty (16) or a spatially varying penalty (17), may improve estimation in those regions by preserving the edges in the field map.
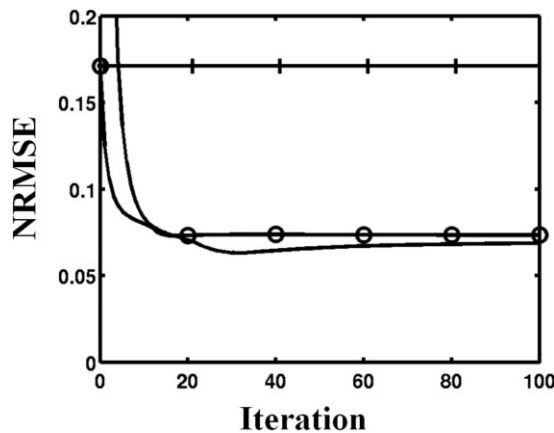

FIG. 4. NRMSE in Hz vs. iteration number for the field map estimation in the axial slice simulation. The solid line (—) indicates the simultaneous estimation initialized with a zero field map, the circles (○) are the simultaneous estimation initialized with the standard field map, and the plus sign (+) is the standard field map estimate, which is not iterative but is shown as a constant value vs. iteration.
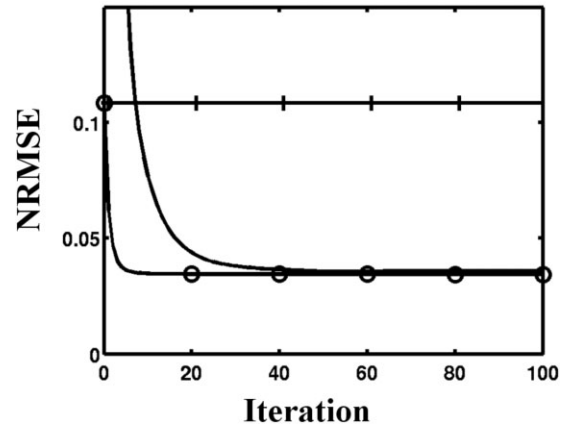

FIG. 5. NRMSE in Hz for the field map estimation in the sagittal slice simulation. The solid line (—) indicates the simultaneous estimation initialized with a zero field map, the circles (○) are the simultaneous estimation initialized with the standard field map, and the plus sign (+) is the standard field map estimate, which is not iterative but is shown as a constant value vs. iteration.

Human Study

A data set was collected during a functional experiment, as described for the human study (subject 1) in the Materials and Methods section, with a TR of 2 s and 80 time points. Field inhomogeneity distortions are generally worse for lower slices of the brain that are closer to the air/tissue interfaces of the sinus cavities. We show results for both a slice low in the brain and a slice containing pixels with significant correlation to the motor task. Figure 7 shows the uncorrected image, the standard and jointly estimated field maps, and the reconstructions obtained with those field maps for a low axial slice at the 10th time point. The T_1-weighted anatomical scan is given for reference. Although the two field maps look similar, the arrows in the reconstructed images indicate positions at which the images show differences in the degree to which inhomogeneity correction was successful. The image reconstructed with the standard field map shows blurring and signal loss at the indicated positions, whereas the increased accuracy
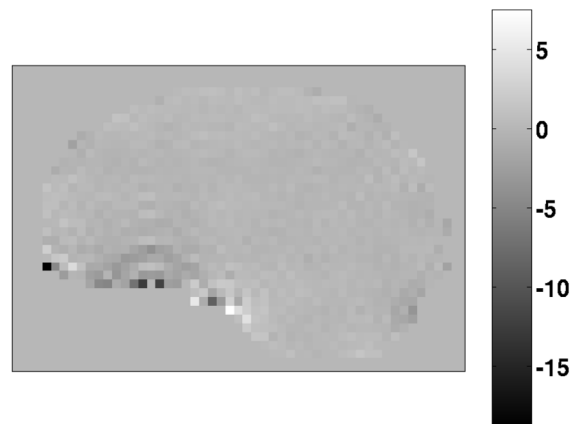

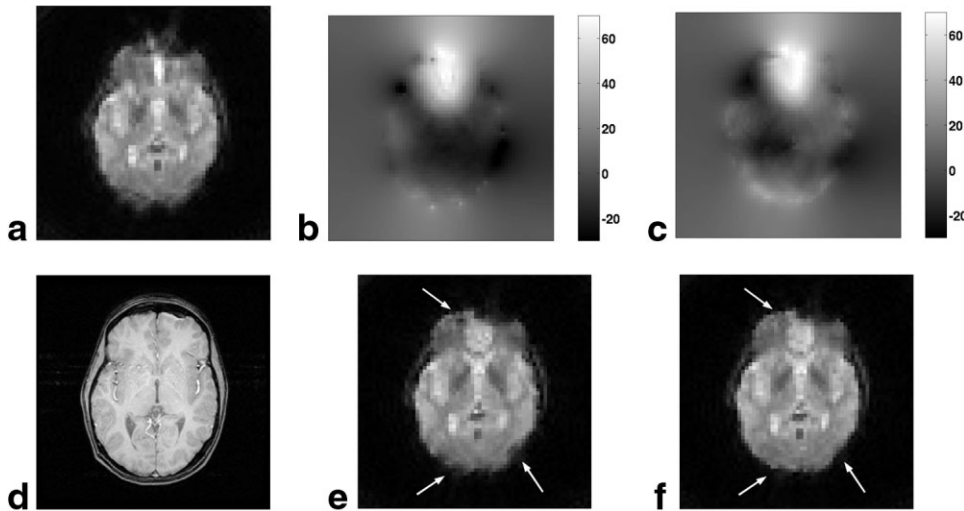FIG. 6. Error in Hz for the sagittal slice.

FIG. 7. Results of reconstruction and estimation on a slice lower in the brain of subject 1: (**a**) uncorrected image, (**b**) standard field map estimate, (**c**) jointly estimated field map, (**d**) T_1 anatomical image for reference, (**e**) image reconstructed using the standard field map, and (**f**) image reconstructed using the jointly estimated field map.

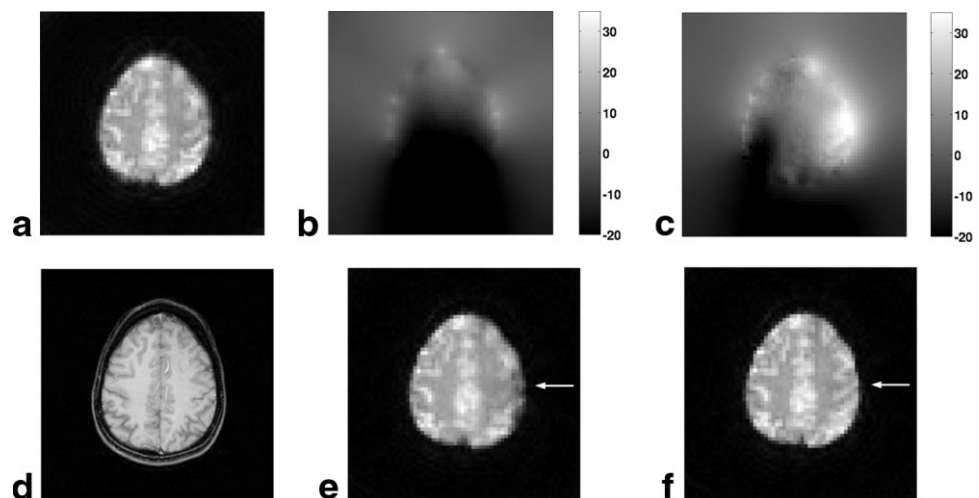of the jointly estimated field map allows for adequate compensation and artifact reduction.

Figure 8 gives the results for the field map estimations and the reconstructed images for a slice containing pixels correlated to the bilateral finger-tapping task. The results for the jointly estimated image and field map are shown for the 10th time point. The standard field map differs considerably from the jointly estimated field map for this slice. Along the edge indicated by the arrow, the reconstructed image with the standard field map shows significant blurring due to field inhomogeneity. The jointly estimated field map and image are largely free of this distortion.
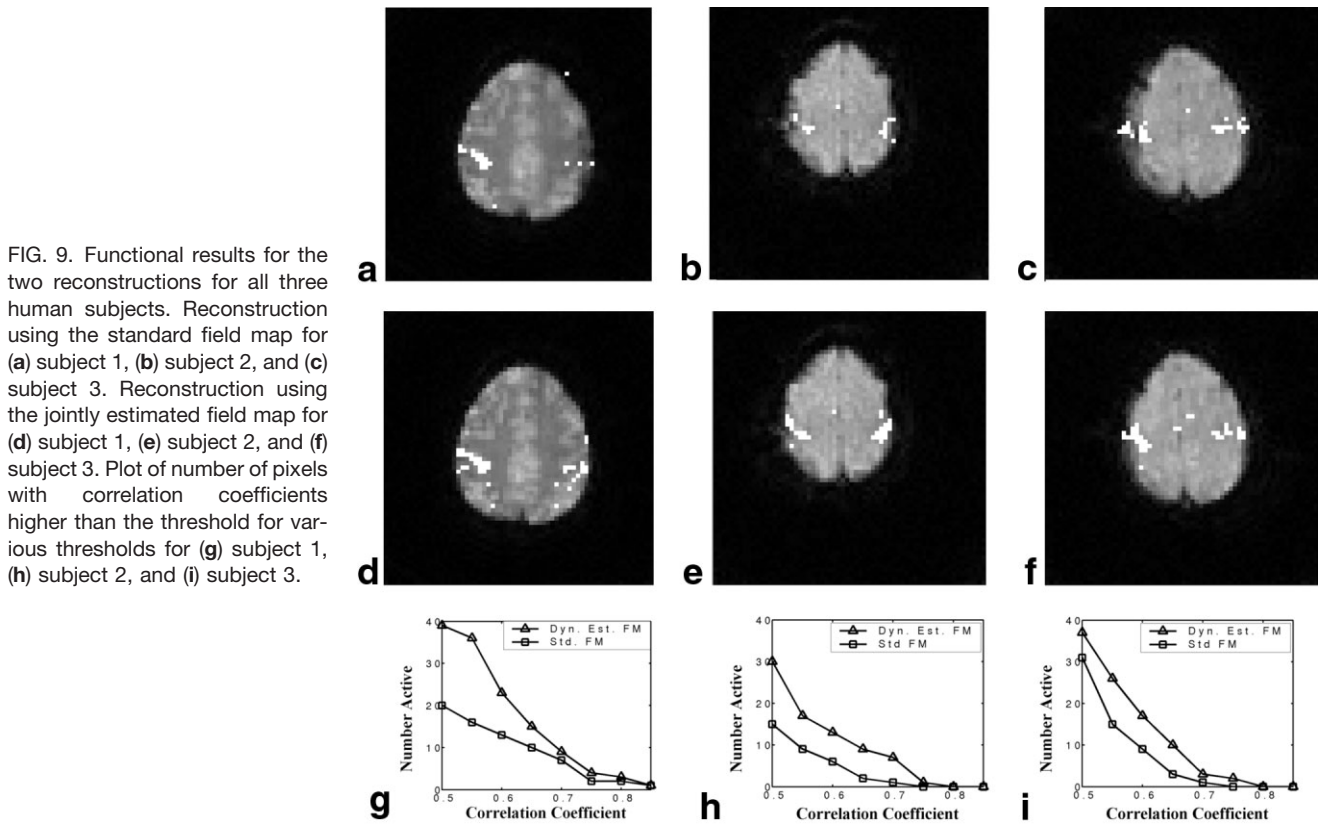
The reduced artifacts obtained with the jointly estimated field map are also evident in the functional results. Figure 9 shows the functional results from reconstructions using the standard and dynamic field maps for all three human subjects examined. Figure 9a–f show the functional activation maps thresholded at a correlation coefficient of 0.5. The reference image shown under the functional map is the image reconstructed using the corresponding method. For subject 1 in Fig. 9a and d, both methods show similar activation on the left-hand side, but only the joint-estimation method shows a comparable number of active voxels on the right-hand side. The increased bilateral detection corresponds with the increased artifact correction (arrow in Fig. 8). Figure 9g shows the number of pixels with correlation coefficients higher than various thresholds for the two reconstructions for subject 1. The trend seen in Fig. 9a and d for a threshold of 0.5 holds for all the other thresholds examined, i.e. a larger number of activated pixels result from correctly compensating for the undistorted, dynamic field map. Figure 9b and d show the functional maps for subject 2 (TR = 0.5 s), and 9c and e show the functional maps for subject 3 (TR = 0.5 s). All maps were thresholded at a correlation coefficient of 0.5. Again we see with both of these subjects that accurate compensation for the dynamic, jointly-estimated field map results in a larger number of activated voxels. The plots of the number of active voxels vs. the threshold level for the two subjects are shown in Fig. 9h and i, respectively.

We can examine the time course of the dynamic, jointly estimated field map at a pixel of interest to study the variance of our field map estimate and identify any main field drift in the scanner. Figure 10 shows the time courses

FIG. 8. Results of reconstruction and estimation on a slice of interest for a functional study of subject 1: (**a**) uncorrected image, (**b**) standard field map estimate, (**c**) jointly estimated field map, (**d**) T_1 anatomical image for reference, (**e**) image reconstructed using the standard field map, and (**f**) image reconstructed using the jointly estimated field map.

FIG. 9. Functional results for the two reconstructions for all three human subjects. Reconstruction using the standard field map for (**a**) subject 1, (**b**) subject 2, and (**c**) subject 3. Reconstruction using the jointly estimated field map for (**d**) subject 1, (**e**) subject 2, and (**f**) subject 3. Plot of number of pixels with correlation coefficients higher than the threshold for various thresholds for (**g**) subject 1, (**h**) subject 2, and (**i**) subject 3.

of the field map estimate of a voxel in the interior region of a phantom and a voxel inside the brain of subject 1. A field drift over the course of the time series exists in both the human and phantom scans (a positive shift in the field of about 2.5 Hz over the course of the 160-s scan). A similar drift in the field map was seen for all pixels inside the phantom and the brain. Such field drifts are seen routinely in our stability scans, and may be due to heating of the passive shims. The field map estimates in the human study have higher oscillations than in the phantom. Regressing out a second-order polynomial fit to the time courses shown in Fig. 10 gives a residual standard deviation (SD) of 0.34 Hz, averaged over the brain, compared to 0.12 Hz averaged over the phantom. Thus our estimation algorithm is fairly stable over the course of a time series, and dynamic estimation allowed us to track a 1-Hz/min drift in the main field strength.

The higher variance in the time series of the field map from the human study compared to the phantom study (Fig. 10) may be due to respiration-induced field changes during the course of the time series. To examine this effect further, two of the subjects were scanned with a TR of 0.5 s to allow for good resolution of the respiratory effect, and a respiratory bellows was used to acquire the respiration waveform. We performed a correlation analysis between the measured respiratory waveform and that from the time course of the estimated field map after we regressed out a second-order polynomial fit to remove the main field drift component. We found that for subject 2, there was a mean correlation coefficient of 0.37 over the brain region between the field map values (after a second-order polyno-
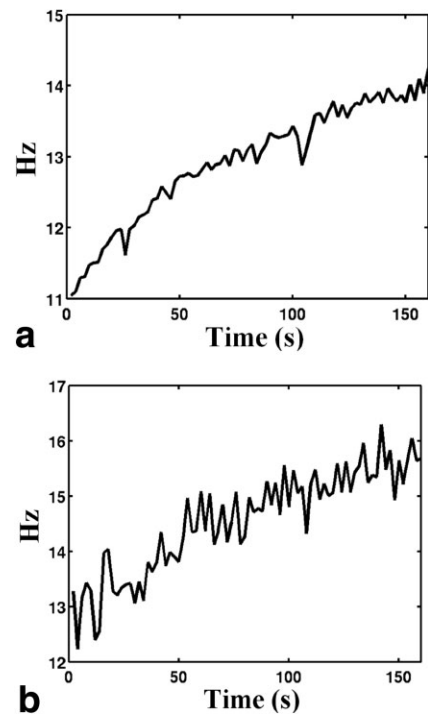

FIG. 10. Time course of a jointly estimated field map for a typical pixel inside (**a**) a phantom and (**b**) a brain.
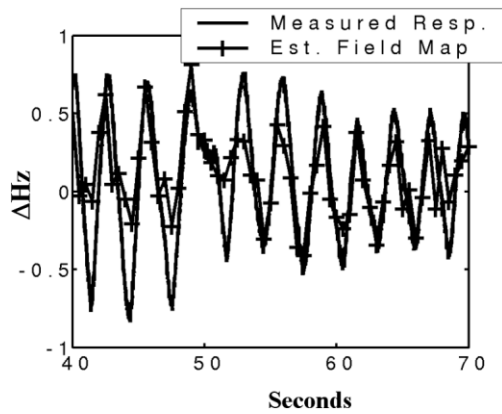
FIG. 11. Plot of the time course of a field map for a pixel inside the brain of subject 3 after a second-order polynomial fit was regressed out to remove the main field drift component. Shown also for reference is a scaled version of the waveform measured from the respiratory bellows.

mial fit was removed) and the respiratory waveform. For subject 3, the mean correlation coefficient over the brain was 0.40. A plot of the time course of the field map for a pixel inside the brain of subject 3 is shown in Fig. 11. This pixel was near the center of the brain and had the highest correlation coefficient with the respiratory waveform (0.79). Also shown in this figure, for reference, is a scaled version of the respiratory waveform as measured from the respiratory bellows. The variations in the field map values are a good fit to the scaled measurements from the respiratory bellows.

Noniterative Dynamic Estimation

At first glance, it might appear that one could form a dynamic field map estimate by first reconstructing uncorrected images from the spiral-in and spiral-out parts of the sequence separately. Since these acquisitions were spaced by 1 ms in our studies, we were able to form a field map by taking the phase difference of these two images and dividing by the difference in TEs. Figure 12 shows the field maps estimated in this manner for the simulation and human experiments. These field maps have shapes that are fairly consistent with the truth (refer to Figs. 1 and 8), but the scaling is wrong, and even results in phase wraps in the field map. The problem with this noniterative dynamic method is that the point spread function of a spiral-in sequence with field inhomogeneity differs greatly from that of a spiral-out acquisition. A possible explanation is

offered in Ref. 8: gradients in the field map distort the local k-space trajectory, which may cause a shift in the timing of the sampling of the center of k-space (the effective TE) that may differ greatly from the planned TE. In the usual case, when spiral-out sequences of the same slice at two different TEs are compared, this effective TE shift is the same for both, which keeps the difference in effective TEs the same as the planned TE delay. However, the time at which the origin of k-space is sampled for spiral-in and spiral-out sequences is affected differently by gradients in the field map. This results in an effective difference in TE between the spiral-in and spiral-out sequences that varies spatially. Without advance knowledge of the true field inhomogeneity distribution or its gradients, we cannot determine this spatially-variant difference in effective TEs. Hence, in addition to the previously mentioned problems associated with the standard field map estimation, field map estimates based on phase differences between spiral-in and spiral-out images are additionally degraded by a spatially-variant scale factor. Note that the simultaneous estimation method presented here is not significantly affected by these gradients.

DISCUSSION

The simulation studies show that our joint estimation technique can estimate a field map that is more accurate than the standard field map estimate. The standard field map estimate requires two acquisitions at slightly different TEs, and assumes that the field map remains static over the course of a time series. Our joint estimation technique uses a spiral-in/spiral-out sequence to estimate an undistorted field map and image at each acquisition. This dynamic estimate was formed with the use of a penalized, least-squares joint-estimation algorithm and a spiral-in/spiral-out acquisition, which does not decrease the scan efficiency from a spiral-out sequence.

The joint estimation algorithm is very stable. For each time point, the algorithm yields an estimate of the field map. By looking at the variance in the time series of the estimated field maps, we can examine the stability of the estimations. In the phantom experiment, the average SD for the time course of the field map was only 0.12 Hz after trends were removed to account for the drift of the magnetic field. The mean SD from the human results was 0.34 Hz. This higher variation resulted from respiration-induced phase variations during the time series. The time series of pixels inside the brain in a slice from two subjects exhibited significant correlation with the respiratory
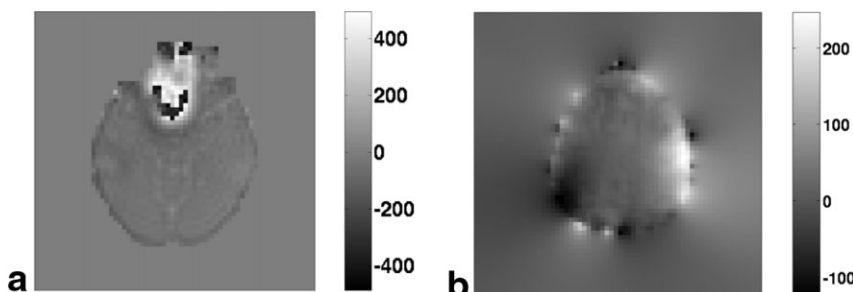

FIG. 12. Field maps estimated from the phase differences of spiral-in and spiral-out images reconstructed separately. **a:** Simulation field map (Hz). **b:** Human field map (Hz).

waveform as measured with a respiratory bellows. A mean correlation coefficient of 0.4 was observed for the time course of the field map with the measured respiratory waveform in a slice high in the brain in two subjects. This respiration effect should be even more significant for slices lower in the brain.

For this work, the accurate measurement of respiratory effects in the time course of the field map attests to the stability and sensitivity of our method. In future studies, the ability of our proposed method to accurately estimate and correct for respiratory noise should be compared with other physiological noise-correction schemes. For example, a technique called dynamic off-resonance in *k*-space (DORK) assumes that respiration-induced phase is constant over the slice (18). This assumption essentially restricts the application of DORK to axial slices. Although our method does use spatial regularization, it does not enforce a uniform shift for the slice. Therefore, our method is applicable to any slice orientation.

Besides the fact that the proposed method is able to track dynamic changes in the field map, the simulation and human experiments suggest that our method results in a more accurate estimate of a single field map. Although the dynamic changes in the field maps over the time series for the human studies were relatively small (<5 Hz), the functional results were dramatically different when the jointly estimated field map was used instead of the standard field map. The jointly estimated field map resulted in an image with less artifact and a higher number of activated voxels in the functional studies. The standard field map estimation method suffers from the use of reference images that are distorted by field inhomogeneity effects, physiologically-induced phase differences, and motion between the reference images.

The joint estimation algorithm can accurately and dynamically track and correct for changes in the field map during the course of the functional study. These changes may be due to respiration-induced phase changes, head movement, and drifts in the center frequency of the magnetic field. These effects will become even more significant at higher field strengths, so dynamic estimation of the field map may be crucial for success of fMRI at high fields. In this work, the subjects were instructed to hold their head still. In patient and pediatric populations, the subjects may not be able to remain still for the time required for a functional study. In these cases, dynamic field map estimation may be necessary for adequate artifact correction and proper estimation of motion-correction parameters. In future studies, we will examine the impact of dynamic field map estimation on motion correction.

Our proposed joint estimation algorithm can be used with any pulse sequence that provides adequate sampling of *k*-space with diversity in TEs to give information about phase accrual. It has also been used with a four-echo spiral-out sequence to jointly estimate the image, field map, and T_2^* relaxation map (19). The spiral-in/spiral-out sequence was chosen for this work because it provides an efficient coverage of *k*-space and allows for a close spacing of TEs. Subsampling strategies, such as those using variable-density spirals (9) or radial lines (10), may allow for a reduction in the acquisition time.

One drawback to the proposed method is computation time. On a 2 GHz Pentium workstation running Matlab, five iterations of the proposed method to estimate an image and a field map took approximately 2 min. Recall that one iteration of our proposed method includes six subiterations of CG on the image and 19 subiterations of gradient descent. Considering that most functional runs have hundreds of time points and multiple slices, this method is computationally expensive for large studies. Multiple processors and dedicated equipment may be necessary to ensure that data can be processed in a timely manner. Some improvement in computation time can be traded for a decrease in accuracy, i.e., reducing the total number of iterations or reducing the number of subiterations for the image and field map updates would decrease the total reconstruction time. A small savings in computation time may be realized by limiting the joint estimation to pixels inside a mask of the brain. It may also be possible to reduce the number of unknowns to be dynamically estimated by limiting the spatial frequencies of the dynamic portion of the field map, similar to the DORK method. Finally, steepest descent is used to update the estimate of the field map. A better algorithm for this nonlinear minimization could significantly reduce computation time.

CONCLUSIONS

We have presented a method to accurately estimate an undistorted image and field map for each acquisition of a spiral-in/spiral-out sequence. This method results in stable field map estimates that are able to track field drift and respiration-induced phase variations over the course of an fMRI time series. In addition to producing dynamic estimates, we have shown that our method can result in better single field map estimates than the standard estimation technique, which is sensitive to differences between the reference images due to subject motion and respiration.

ACKNOWLEDGMENTS

REFERENCES

1. Ogawa S, Tank DW, Menon R, Ellerman JM, Kim S-G, Merkle H, Ugurbil K. Intrinsic signal changes accompanying sensory stimulation: functional brain mapping with magnetic resonance imaging. Proc Natl Acad Sci USA 1992;89:5951–5955.
2. Noll DC, Meyer CH, Pauly JM, Nishimura DG, Macovski A. A homogeneity correction method for magnetic resonance imaging with time-varying gradients. IEEE Trans Med Imaging 1991;10:629–637.
3. Noll DC, Pauly JM, Meyer CH, Nishimura DG, Macovski A. Deblurring for non-2D Fourier transform magnetic resonance imaging. Magn Reson Med 1992;25:319–333.
4. Kadah YM, Hu X. Simulated phase evolution rewinding (SPHERE): a technique for reducing Bo inhomogeneity effects in MR images. Magn Reson Med 1997;38:615–627.
5. Schomberg H. Off-resonance correction of MR images. IEEE Trans Med Imaging 1999;18:481–495.
6. Man L-C, Pauly JM, Macovski A. Multifrequency interpolation for fast off-resonance correction. Magn Reson Med 1997;37:785–792.
7. Schneider E, Glover G. Rapid in vivo proton shimming. Magn Reson Med 1991;18:335–347.

8. Noll DC. Rapid MR image acquisition in the presence of background gradients. In: Proceedings of the 1st IEEE International Symposium on Biomedical Imaging, Washington, D.C., 2002. p 725−728.

9. Nayak KS, Tsai C-M, Meyer CH, Nishimura DG. Efficient off-resonance correction for spiral imaging. Magn Reson Med 2001;45:521−524.

10. Nayak KS, Nishimura DG. Automatic field map generation and off-resonance correction for projection reconstruction imaging. Magn Reson Med 2000;43:151−154.

11. Glover GH, Law CS. Spiral in/out BOLD fMRI for increased SNR and reduced susceptibility artifacts. Magn Reson Med 2001;46:515−522.

12. Sutton BP, Noll DC, Fessler JA. Fast, iterative, field-corrected image reconstruction for MRI. IEEE Trans Med Imaging 2003;22:178−188.

13. Fessler JA, Sutton BP. Nonuniform fast Fourier transforms using min-max interpolation. IEEE Trans Signal Proc 2003;51:560−574.

14. Haacke EM, Brown RW, Thompson MR, Venkatesan R. Magnetic resonance imaging: physical principles and sequence design. New York: John Wiley and Sons; 1999.

15. Fessler JA. Penalized weighted least-squares image reconstruction for positron emission tomography. IEEE Trans Med Imaging 1994;13:290−300.

16. Huber PJ. Robust statistics. New York: Wiley; 1981.

17. Stayman JW, Fessler JA. Regularization for uniform spatial resolution properties in penalized-likelihood image reconstruction. IEEE Trans Med Imaging 2000;19:601−615.

18. Pfeuffer J, Van de Moortele P-F, Urgurbil K, Hu X, Glover GH. Correction of physiologically-induced global off-resonance effects in dynamic echo-planar and spiral functional imaging. Magn Reson Med 2002;47:344−353.

19. Sutton BP, Peltier SJ, Fessler JA, Noll DC. Simultaneous estimation of Io, R2*, and field map using a multi-echo spiral acquisition. In: Proceedings of the 10th Annual Meeting of ISMRM, Honolulu, 2002. p 1323.